Aalto University

OPEN ACCESS

This is an electronic reprint of the original article.
This reprint may differ from the original in pagination and typographic detail.

Sokolov, Maksim; Saarakkala, Seppo E.; Hosseinzadeh, Reza; Hinkkanen, Marko

A dynamic model for bearingless flux-switching permanent-magnet linear machines

Published in:
IEEE Transactions on Energy Conversion

DOI:
10.1109/TEC.2020.2975082

Published: 19/02/2020

Document Version
Peer-reviewed accepted author manuscript, also known as Final accepted manuscript or Post-print

Please cite the original version:
Sokolov, M., Saarakkala, S. E., Hosseinzadeh, R., & Hinkkanen, M. (2020). A dynamic model for bearingless flux-switching permanent-magnet linear machines. *IEEE Transactions on Energy Conversion*, *35*(3), 1218-1227. Article 9003283. https://doi.org/10.1109/TEC.2020.2975082

This material is protected by copyright and other intellectual property rights, and duplication or sale of all or part of any of the repository collections is not permitted, except that material may be duplicated by you for your research use or educational purposes in electronic or print form. You must obtain permission for any other use. Electronic or print copies may not be offered, whether for sale or otherwise to anyone who is not an authorised user.

A Dynamic Model for Bearingless Flux-Switching Permanent-Magnet Linear Machines

Maksim Sokolov, Seppo E. Saarakkala, Reza Hosseinzadeh, and Marko Hinkkanen, *Senior Member, IEEE*

***Abstract*—This paper deals with dynamic models for three-phase bearingless flux-switching permanent-magnet (FSPM) linear machines. This machine type can be used to build a magnetically levitating long-range linear drive system, whose rail does not need any active materials apart from iron. A dynamic machine model is developed by means of equivalent magnetic models, taking into account air-gap variation and magnetic saturation. The effects of these phenomena are analyzed using finite-element method (FEM) simulations of a test machine. The parameters of the proposed model can be identified using the FEM or measured data. The model can be applied to real-time control and time-domain simulations. The model is validated by means of experiments.**

***Index Terms*—Bearingless, flux-switching permanent-magnet (FSPM) machine, linear least squares (LLS), linear motor, magnetic levitation, magnetic model, modeling.**

I. Introduction

A ROTATING flux-switching permanent-magnet (FSPM) machine has a very simple rotor structure, due to its permanent magnets (PMs) and three-phase concentrated winding being located in the stator [1], [2]. This machine type has comparatively high power density. Its back-emf phase voltages are almost sinusoidal. A typical configuration has 12 stator teeth and 10 rotor poles (12/10). Recently, a bearingless version of the FSPM machine has been developed [3]. In addition to torque production, bearingless machines also produce a radial force, which can be controlled to allow for contactless operation of the machine. A multiphase winding structure is used in bearingless machines to produce an uneven flux density in the air gap, which creates an unbalanced magnetic pull on the rotor [4].

Linear variants [5] of the FSPM machine have become an interesting option for producing the thrust force in various applications, such as traction [6], wave-energy generation [7], urban rail transit [8], electromagnetic launch systems [9], and elevator systems [10], [11]. The linear FSPM machine has both magnets and windings in the same part of the machine. Hence, in traction applications, the rail or track along which the mover travels does not need any active materials apart from iron, which significantly reduces the costs. The windings located in the mover have to be energized, which requires implementing energy transfer to the mover or using on-board batteries. Like their rotating counterparts, FSPM linear machines can be modeled and controlled using two-axis models [8]. Various analytical and semi-analytical models have been presented for machine design and analysis purposes [12], [13].

This work was supported by the KONE Corporation.

M. Sokolov, S. E. Saarakkala, R. Hosseinzadeh, and M. Hinkkanen are with the Department of Electrical Engineering and Automation, Aalto University, Espoo, Finland (e-mail: maksim.sokolov@aalto.fi; seppo.saarakkala@aalto.fi; reza.hosseinzadeh@aalto.fi; marko.hinkkanen@aalto.fi).

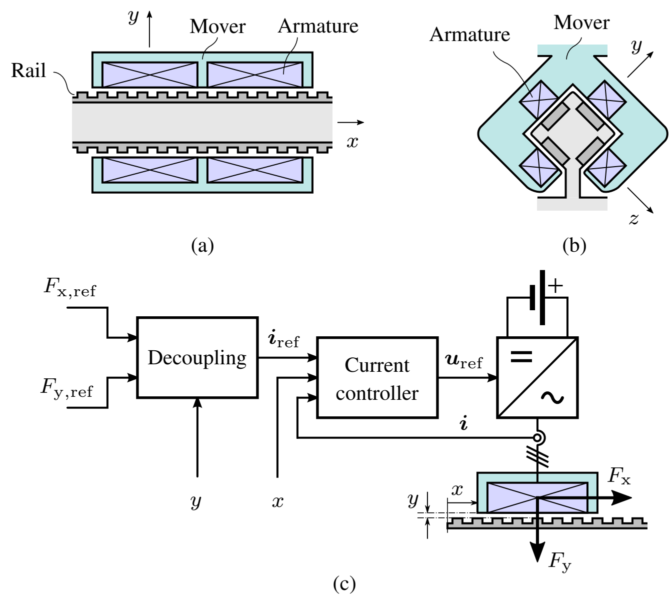

Fig. 1. Example configuration of a bearingless linear drive system, consisting of a beam with rails and a mover with eight machine units: (a) cross-section in the xy plane; (b) cross-section in the yz plane; (c) decoupled force controller for a single machine unit. The thrust-force reference $F_{\mathrm{x,ref}}$ is obtained from the traction controller and the normal-force reference $F_{\mathrm{y,ref}}$ from the levitation controller.

In addition to the thrust force, FSPM linear machines produce the normal force that pulls the mover toward the rail. Since this attraction force is large, the linear machines typically have a double-sided or four-sided structure to balance the magnetic pull on both sides of the rail [7]. A bearingless version of the FSPM linear machine can be created by actively controlling the attraction force to maintain a desired air gap [14].

A magnetically levitating drive system may consist of bearingless FSPM linear machine units [11], [15]. The machine units can be arranged in various ways. Figs. 1(a) and (b) illustrate an example configuration, where motion in the x direction is produced and the remaining five degrees of freedom are stabilized. Fig. 1(c) shows an example force controller for a single machine unit. Active magnetic levitation presents a challenge from the control point of view. The open-loop system is unstable and highly nonlinear due to varying air gap and magnetic saturation. The development of the control system requires suitable machine models, which take the air-gap variation and magnetic saturation properly into account.

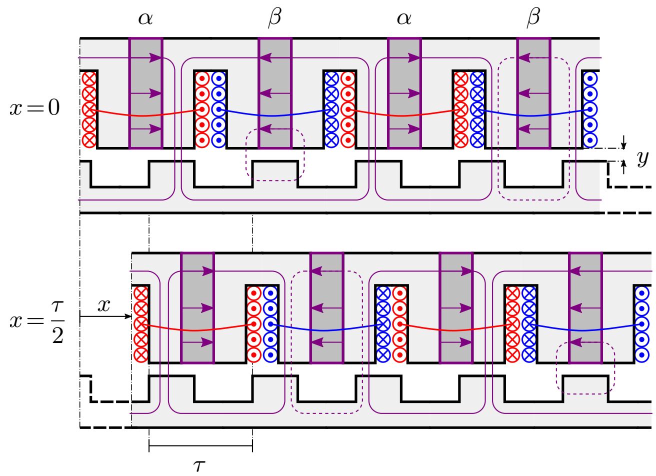

Fig. 2. Conceptual two-phase FSPM linear machine, the mover positioned at $x = 0$ and at $x = \tau/2$. The polarities of the PMs (placed between the coils) are shown by the arrows. The crosses and dots define the positive direction of the coil currents. The phases α and β are labeled above the corresponding coils. The most significant flux paths due to the PMs are also sketched. The flux paths marked with the dashed lines do not link with the coils.

In this paper, we develop an analytical dynamic model for bearingless three-phase FSPM linear machines. The model is intended for control design, stability analyses, time-domain simulations, and real-time control. The main contributions of this paper are:

1) A magnetic equivalent circuit is proposed and used to derive analytical equations describing the magnetic model and the force production. The corresponding state equations needed for the dynamic model are presented.
2) Using the finite-element method (FEM), the magnetic characteristics of an example two-phase machine and a prototype three-phase machine are analyzed, including the influence of the air-gap variation, x-axis position dependency, and magnetic saturation.
3) A simple method for estimating the parameters of the proposed model from the FEM or measured data is presented.

The proposed model is validated by means of experiments. As compared to our earlier conference paper [16], we apply a physically more feasible equivalent circuit, which leads to improvements in the resulting magnetic model. The effect of the air gap on the saturation state is studied in more detail. Furthermore, we present new FEM and experimental results. It is also to be noted that a control system based on the developed model as well as experimental results of levitation and propulsion tests were recently presented in [15].

II. Generic Dynamic Model

To provide a solid basis, we first introduce a generic dynamic model based on the fundamental principles of electromechanical energy conversion [17], [18]. A three-phase bearingless FSPM linear machine, consisting of a toothed rail and a mover, is considered. The rail is composed of electric steel sheets. The mover includes both the PMs and a three-phase winding. The core losses of the machine are omitted (but they could be taken into account separately, if needed).

A. $\alpha\beta$ Coordinates

Since the three-phase winding is either delta-connected or the star point is not connected, the zero-sequence current cannot flow. Therefore, the zero-sequence components cannot contribute to the power or forces, and an equivalent two-phase $\alpha\beta$ model can be used. Using the phase currents i_a, i_b, and i_c as an example, the $\alpha\beta$ components are obtained as

$$\begin{bmatrix} i_\alpha \\ i_\beta \end{bmatrix} = \sqrt{\frac{2}{3}} \begin{bmatrix} 1 & -1/2 & -1/2 \\ 0 & \sqrt{3}/2 & -\sqrt{3}/2 \end{bmatrix} \begin{bmatrix} i_\mathrm{a} \\ i_\mathrm{b} \\ i_\mathrm{c} \end{bmatrix} \tag{1}$$

where power-invariant scaling is used. The same transformation applies to the flux linkages and the voltages.

Fig. 2 illustrates a conceptual model of a two-phase FSPM linear machine with the simple 4-slot/5-pole configuration. This model includes essentially the same phenomena as encountered in three-phase machines. Therefore, to avoid adding too much complexity, we apply the conceptual model to explain the key concepts. The dominant flux paths of the PMs are sketched in Fig. 2. When the mover is positioned at $x = 0$, the PM flux linking with the α-phase coils has its maximum value, while no flux links with the β-phase coils. It can be seen that the polarity of the phase flux linkage ψ_α is reversed, as the mover travels from $x = 0$ to $x = \tau/2$, where τ is the pole pitch of the rail. It can also be seen that some PM flux paths do not link with the windings. These PM leakage fluxes cannot be observed from the electrical terminals, but they contribute to the magnetic field energy.

Fig. 3(a) shows a generic lumped-element dynamic model for the bearingless linear machine in $\alpha\beta$ coordinates. The voltage equations are

$$\frac{\mathrm{d}\psi_\alpha}{\mathrm{d}t} = u_\alpha - R i_\alpha \qquad \frac{\mathrm{d}\psi_\beta}{\mathrm{d}t} = u_\beta - R i_\beta \tag{2}$$

where ψ_α, ψ_β are the flux-linkage components, u_α, u_β are the voltage components, and R is the resistance. In the general case, the currents can be expressed as

$$i_\alpha = i_\alpha(\psi_\alpha, \psi_\beta, x, y) \qquad i_\beta = i_\beta(\psi_\alpha, \psi_\beta, x, y) \tag{3}$$

where y is the air gap. Alternatively, the reciprocal relationships $\psi_\alpha = \psi_\alpha(i_\alpha, i_\beta, x, y)$ and $\psi_\beta = \psi_\beta(i_\alpha, i_\beta, x, y)$ could be used. However, choosing the flux linkages as independent state variables in (3) simplifies inclusion of the magnetic saturation in the model. Furthermore, this choice allows the voltage equations to be kept in their simplest possible form.

In accordance with Fig. 3(a), the rate of change of the magnetic field energy W is

$$\frac{\mathrm{d}W}{\mathrm{d}t} = i_\alpha \frac{\mathrm{d}\psi_\alpha}{\mathrm{d}t} + i_\beta \frac{\mathrm{d}\psi_\beta}{\mathrm{d}t} - F_\mathrm{x} \frac{\mathrm{d}x}{\mathrm{d}t} - F_\mathrm{y} \frac{\mathrm{d}y}{\mathrm{d}t}. \tag{4}$$

Since the coupling magnetic field is assumed to be lossless, the thrust and normal forces, respectively, are [17], [18]

$$F_\mathrm{x} = -\frac{\partial W(\psi_\alpha, \psi_\beta, x, y)}{\partial x} \qquad F_\mathrm{y} = -\frac{\partial W(\psi_\alpha, \psi_\beta, x, y)}{\partial y}. \tag{5}$$

It is to be noted that the magnetic field energy W is generally nonzero at $\psi_\alpha = \psi_\beta = 0$ due to the PM leakage fluxes.

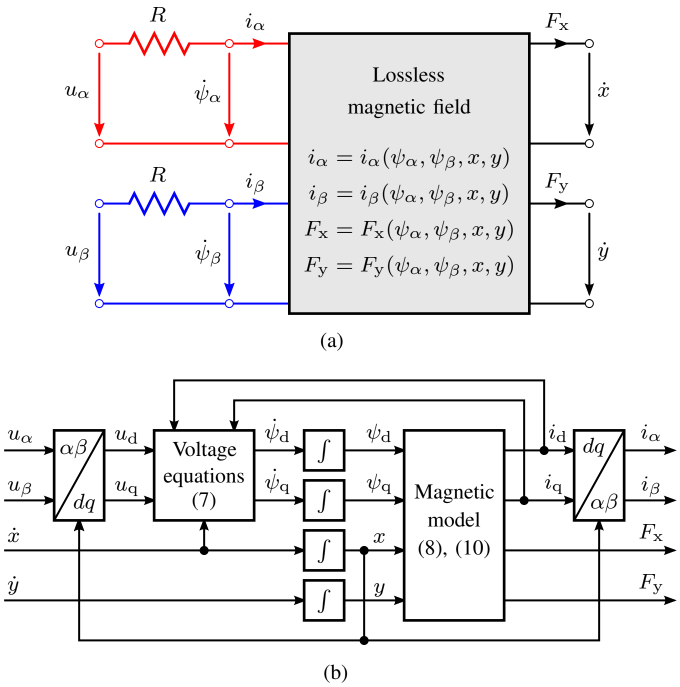

Fig. 3. Generic dynamic model for a bearingless linear machine: (a) equivalent circuit model in $\alpha\beta$ coordinates; (b) corresponding block diagram in dq coordinates. Time derivatives are marked with the dots.

B. *dq Coordinates*

FSPM machines can be effectively modeled in dq coordinates, as demonstrated in the pioneering paper [1]. The model in $\alpha\beta$ coordinates can be transformed to dq coordinates with no loss of information. As an example, the current components are transformed to dq coordinates using

$$\begin{bmatrix} i_\mathrm{d} \\ i_\mathrm{q} \end{bmatrix} = \begin{bmatrix} \cos(\vartheta_\mathrm{m}) & \sin(\vartheta_\mathrm{m}) \\ -\sin(\vartheta_\mathrm{m}) & \cos(\vartheta_\mathrm{m}) \end{bmatrix} \begin{bmatrix} i_\alpha \\ i_\beta \end{bmatrix} \tag{6}$$

where the position x of the mover with respect to the rail is expressed in radians as $\vartheta_\mathrm{m} = 2\pi x/\tau$. The flux linkages and the voltages are transformed similarly.

The voltage equations (2) transformed to dq coordinates are

$$\frac{\mathrm{d}\psi_\mathrm{d}}{\mathrm{d}t} = u_\mathrm{d} - Ri_\mathrm{d} + \omega_\mathrm{m}\psi_\mathrm{q} \tag{7a}$$
$$\frac{\mathrm{d}\psi_\mathrm{q}}{\mathrm{d}t} = u_\mathrm{q} - Ri_\mathrm{q} - \omega_\mathrm{m}\psi_\mathrm{d} \tag{7b}$$

where ψ_d, ψ_q are the flux-linkage components, u_d, u_q are the voltage components, and $\omega_\mathrm{m} = (2\pi/\tau) \cdot (\mathrm{d}x/\mathrm{d}t)$ is the electrical angular speed. The currents can be expressed as functions of the new state variables,

$$i_\mathrm{d} = i_\mathrm{d}(\psi_\mathrm{d}, \psi_\mathrm{q}, x, y) \qquad i_\mathrm{q} = i_\mathrm{q}(\psi_\mathrm{d}, \psi_\mathrm{q}, x, y). \tag{8}$$

Applying the coordinate transformations to (4) leads to

$$\frac{\mathrm{d}W}{\mathrm{d}t} = i_\mathrm{d}\left(\frac{\mathrm{d}\psi_\mathrm{d}}{\mathrm{d}t} - \omega_\mathrm{m}\psi_\mathrm{q}\right) + i_\mathrm{q}\left(\frac{\mathrm{d}\psi_\mathrm{q}}{\mathrm{d}t} + \omega_\mathrm{m}\psi_\mathrm{d}\right) - F_\mathrm{x}\frac{\mathrm{d}x}{\mathrm{d}t} - F_\mathrm{y}\frac{\mathrm{d}y}{\mathrm{d}t} \tag{9}$$

which directly yields the expressions for the thrust and normal forces, respectively,

$$F_\mathrm{x} = -\frac{\partial W(\psi_\mathrm{d}, \psi_\mathrm{q}, x, y)}{\partial x} + \frac{2\pi}{\tau}(\psi_\mathrm{d} i_\mathrm{q} - \psi_\mathrm{q} i_\mathrm{d}) \tag{10a}$$
$$F_\mathrm{y} = -\frac{\partial W(\psi_\mathrm{d}, \psi_\mathrm{q}, x, y)}{\partial y} \tag{10b}$$

expressed by means of dq variables. Fig. 3(b) shows the block diagram representation of the generic model in dq coordinates. The coordinate transformations between the $\alpha\beta$ and dq coordinates are also shown. This electrical subsystem model is easy to supplement with a mechanical subsystem model: the forces F_x and F_y are the inputs and the speeds $\mathrm{d}x/\mathrm{d}t$ and $\mathrm{d}y/\mathrm{d}t$ are the outputs of the mechanical subsystem model.

In well-designed linear machines, the spatial harmonics and the end effects are minor and can be omitted in the dynamic models.[1] Correspondingly, the remaining part of this paper assumes that the model in dq coordinates is independent of x. Therefore, the currents are of the form

$$i_\mathrm{d} = i_\mathrm{d}(\psi_\mathrm{d}, \psi_\mathrm{q}, y) \qquad i_\mathrm{q} = i_\mathrm{q}(\psi_\mathrm{d}, \psi_\mathrm{q}, y) \tag{11}$$

and the field energy is of the form $W = W(\psi_\mathrm{d}, \psi_\mathrm{q}, y)$. The thrust-force expression reduces to

$$F_\mathrm{x} = \frac{2\pi}{\tau}(\psi_\mathrm{d} i_\mathrm{q} - \psi_\mathrm{q} i_\mathrm{d}). \tag{12}$$

The expression for the normal force reduces to

$$F_\mathrm{y} = -\frac{\partial W(\psi_\mathrm{d}, \psi_\mathrm{q}, y)}{\partial y}. \tag{13}$$

Even if the air gap y is not directly visible in (12), the thrust-force production of the bearingless machine depends on the air-gap value via the current components in (11).

C. *Example Two-Phase Machine*

To illustrate some characteristics of bearingless FSPM linear machines, a simple two-phase machine is used as an example in this subsection. Fig. 4(a) shows the flux density at $x = 0$ and $i_\alpha = i_\beta = 0$, solved using the FEM. At this position, the flux linkage ψ_α has its maximum value and the flux linkage $\psi_\beta = 0$. Fig. 4(b) shows the phase flux linkages as a function of x. It can be seen that the flux linkages vary almost sinusoidally even for this simple machine.

Fig. 4(c) shows the flux linkages as a function of the air gap y at constant currents and constant x. At small air-gap values, the PM flux saturates the parts of the iron that the q-axis flux passes through, as can be seen in Fig. 4(a). As the air gap increases from zero, the saturation caused by the PM flux decreases, which explains the increase in ψ_q. After approximately $y = 4$ mm, the iron comes out of the saturation and the effect of the decreasing ψ_q with increasing air gap becomes predominant. In the d-axis, this effect is not visible, since the PM flux is contributing to ψ_d, which always has a negative slope with respect to the air gap. In Fig. 4(c), the

[1] This assumption underlies most dynamic machine models presented in the literature [18], including the model for regular FSPM machines [1] and the textbook models for various bearingless machines [4].

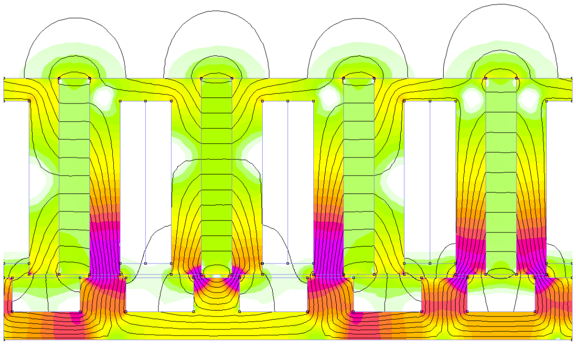

(a)

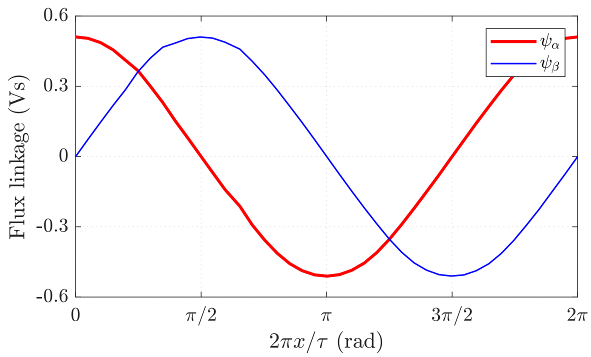

(b)

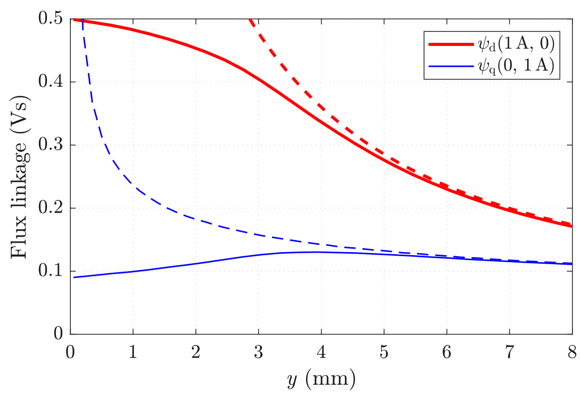

(c)

Fig. 4. FEM results for an example two-phase machine: (a) flux density produced by the PMs at $x = 0$ and $i_\alpha = i_\beta = 0$; (b) $\alpha\beta$ flux linkages as a function of the position x at $i_\alpha = i_\beta = 0$; (c) flux linkage components at constant currents plotted as a function of the air gap y (increasing far beyond the nominal value for illustration purposes). In (c), the dashed lines show the flux linkages obtained with a linear BH curve for iron.

dashed lines show the FEM results produced with a linear BH curve for the iron. This comparison highlights the effect of the saturation on the flux linkages especially at low air-gap values.

Fig. 4(a) also shows that some PM flux paths do not link with the coils but cross the air gap, as already mentioned in connection with the conceptual machine in Fig. 2. Since these PM leakage fluxes depend on the air-gap length y, they contribute to the magnetic field energy and the normal-force production.

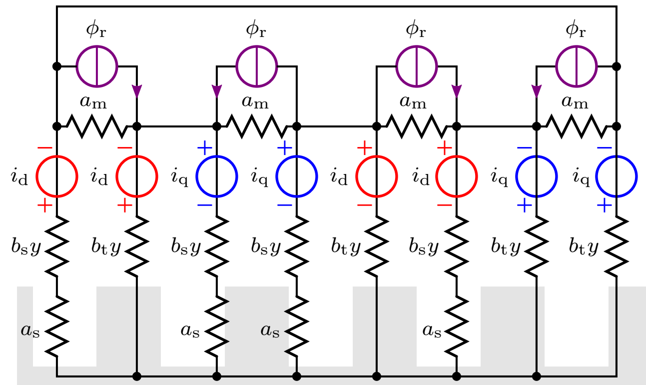

Fig. 5. Simplified magnetic equivalent circuit of the conceptual machine. This circuit is used to derive the proposed magnetic model. The reluctance of the tooth is $b_\mathrm{t}y$ and the reluctance of the slot is $a_\mathrm{s} + b_\mathrm{s}y$, where a_s, b_s, and b_t are assumed to be constants. For simplicity, unity turns are assumed in the circuit.

III. Proposed Magnetic Model

The proposed magnetic model is developed in dq coordinates, where the voltage equations are given by (7). As already mentioned, the spatial harmonics are omitted. Since the PM flux links only with the d-axis winding, the currents (11) can be expressed in a more specific form

$$i_\mathrm{d} = \mathit{\Gamma}_\mathrm{d}(\psi_\mathrm{d}, \psi_\mathrm{q}, y)\psi_\mathrm{d} - i_\mathrm{m}(y) \tag{14a}$$

$$i_\mathrm{q} = \mathit{\Gamma}_\mathrm{q}(\psi_\mathrm{d}, \psi_\mathrm{q}, y)\psi_\mathrm{q} \tag{14b}$$

where $\mathit{\Gamma}_\mathrm{d}$ and $\mathit{\Gamma}_\mathrm{q}$ are the inverse inductances and i_m is the equivalent magnetomotive force (MMF) of the PMs seen from the terminals. The inverse inductances and the equivalent MMF depend on the air gap y. The inverse inductances may also depend on the flux linkages due to the magnetic saturation. The magnetic field energy at $\psi_\mathrm{d} = \psi_\mathrm{q} = 0$ depends on the air gap and is denoted by $w_0 = w_0(y)$. This field energy is nonzero due to the PM leakage fluxes. In order to find suitable algebraic forms for the functions $\mathit{\Gamma}_\mathrm{d}$, $\mathit{\Gamma}_\mathrm{q}$, i_m, and w_0, magnetic equivalent circuits are considered in the following subsection.

A. Magnetically Linear Case

First, the magnetic saturation is omitted. A simplified magnetic equivalent circuit shown in Fig. 5 is considered. This circuit is formed based on the dominant flux paths of the conceptual machine shown in Fig. 2. Without loss of generality, unity turns for the coil MMFs are assumed. The PMs are modeled using the Norton equivalent circuit [19], consisting of the internal reluctance a_m and the remanent flux ϕ_r of the magnet, which are both constant. The constant reluctance a_s models the reluctance between the rail poles. The reluctances $b_\mathrm{s}y$ and $b_\mathrm{t}y$ depend on the air gap, b_s and b_t being constants.

For the circuit in Fig. 5, the inverse inductances $\mathit{\Gamma}_\mathrm{d}(y)$ and $\mathit{\Gamma}_\mathrm{q}(y)$ and the equivalent MMF $i_\mathrm{m}(y)$ are rational functions of the air gap y, as shown in the Appendix. Using (14), the total magnetic field energy can be solved [17], [18]

$$W = \frac{\mathit{\Gamma}_\mathrm{d}(y)\psi_\mathrm{d}^2 + \mathit{\Gamma}_\mathrm{q}(y)\psi_\mathrm{q}^2}{2} - i_\mathrm{m}(y)\psi_\mathrm{d} + w_0(y). \tag{15}$$

The magnetic field energy w_0 at $\psi_\mathrm{d} = \psi_\mathrm{q} = 0$ is of the form

$$w_0(y) = \frac{\mathit{\Gamma}_\mathrm{d}(y)\psi_\mathrm{d0}(y)^2}{2} + \frac{fy}{1+cy} \tag{16}$$

where c and f are constants and $\psi_\mathrm{d0}(y)$ is the d-axis flux linkage at $i_\mathrm{d} = 0$, i.e.,

$$\psi_\mathrm{d0}(y) = \frac{i_\mathrm{m}(y)}{\mathit{\Gamma}_\mathrm{d}(y)}. \tag{17}$$

The last term in (16) is the field energy at $i_\mathrm{d} = i_\mathrm{q} = 0$. It is worth noticing that the equivalent MMF i_m has an effect on both the total field energy W in (15) and the field energy term w_0 in (16). The analytical expression for the normal force can be calculated using (13) and (15). However, the force expression becomes very long in the case of rational functions.

To simplify and generalize the model, we approximate the rational functions $\mathit{\Gamma}_\mathrm{d}(y)$, $\mathit{\Gamma}_\mathrm{q}(y)$, and $i_\mathrm{m}(y)$ with their series expansion at $y = 0$. Typically, the first-order expansion suffices for the inverse inductances and the second-order expansion is required for the equivalent MMF, i.e.,

$$\mathit{\Gamma}_\mathrm{d}(y) = a_\mathrm{d} + b_\mathrm{d} y \tag{18a}$$
$$\mathit{\Gamma}_\mathrm{q}(y) = a_\mathrm{q} + b_\mathrm{q} y \tag{18b}$$
$$i_\mathrm{m}(y) = i_\mathrm{m0} + b_\mathrm{m} y + b'_\mathrm{m} y^2 \tag{18c}$$

where a_d, a_q, b_d, b_q, i_m0, b_m, and b'_m are constants. The constants can be fitted based on the FEM or measured data. Alternatively, they could be approximated by means of a magnetic equivalent circuit, whose reluctances are calculated using the geometry. Applying (13), (15), and (18), the normal force expression becomes

$$F_\mathrm{y} = -\frac{b_\mathrm{d}\left[\psi_\mathrm{d}^2 - \psi_\mathrm{d0}(y)^2\right] + b_\mathrm{q}\psi_\mathrm{q}^2}{2} + (b_\mathrm{m} + 2b'_\mathrm{m} y)[\psi_\mathrm{d} - \psi_\mathrm{d0}(y)] - \frac{f}{(1+cy)^2}. \tag{19}$$

The voltage equations (7) together with the magnetic model consisting of (12), (14), (18), and (19) describe the dynamic model of the bearingless FSPM linear machine in the magnetically linear case. Furthermore, the block diagram shown in Fig. 3(b) is valid and directly applicable with the above-mentioned magnetic model.

B. Inclusion of the Magnetic Saturation

The effects of the magnetic saturation are modeled as a function of the flux linkage magnitude by adding the same nonlinear reluctance term to the d- and q-axis inverse inductances, i.e.,

$$\mathit{\Gamma}_\mathrm{d}(\psi_\mathrm{d}, \psi_\mathrm{q}, y) = a_\mathrm{d} + b_\mathrm{d} y + a_\mathrm{c}(\psi_\mathrm{d}^2 + \psi_\mathrm{q}^2) \tag{20a}$$
$$\mathit{\Gamma}_\mathrm{q}(\psi_\mathrm{d}, \psi_\mathrm{q}, y) = a_\mathrm{q} + b_\mathrm{q} y + a_\mathrm{c}(\psi_\mathrm{d}^2 + \psi_\mathrm{q}^2) \tag{20b}$$
$$i_\mathrm{m}(y) = i_\mathrm{m0} + b_\mathrm{m} y + b'_\mathrm{m} y^2 \tag{20c}$$

where a_c is constant. Similar saturation models have been used in [20], [21]. It can be shown that the reciprocity condition $\partial i_\mathrm{d}/\partial\psi_\mathrm{q} = \partial i_\mathrm{q}/\partial\psi_\mathrm{d}$ holds, i.e., the nonlinear magnetic circuit is lossless [17]. If needed, the saturation model could be elaborated by including separate reluctance terms for self-axis and cross-axis saturation [21].

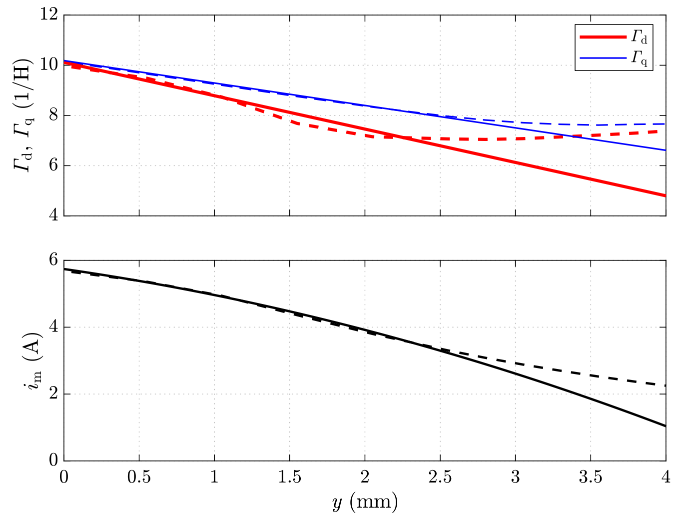

Fig. 6. Inverse inductances and equivalent MMF at constant flux linkages as functions of the air gap for the two-phase example machine. The dashed lines show the FEM results. The solid lines show the results from the model (20), fitted to the FEM data.

The total magnetic field energy corresponding to (20) can be expressed as

$$W = \frac{\mathit{\Gamma}_\mathrm{d}(\psi_\mathrm{d}, \psi_\mathrm{q}, y)\psi_\mathrm{d}^2 + \mathit{\Gamma}_\mathrm{q}(\psi_\mathrm{d}, \psi_\mathrm{q}, y)\psi_\mathrm{q}^2}{2} - i_\mathrm{m}(y)\psi_\mathrm{d} - \frac{a_\mathrm{c}(\psi_\mathrm{d}^2 + \psi_\mathrm{q}^2)^2}{4} + w_0(y) \tag{21}$$

where the field energy function w_0 at $\psi_\mathrm{d} = \psi_\mathrm{q} = 0$ generally differs from the magnetically linear case, cf. (15). However, for simplicity, we assume w_0 equal to the linear case. Under this assumption, the normal force expression (19) is still valid, if $\psi_\mathrm{d0}(y)$ is calculated using the linear inverse inductance $\mathit{\Gamma}_\mathrm{d}(y)$ given in (18a). It is worth noticing that the nonlinear magnetic circuit is physically consistent despite this assumption. In case $a_\mathrm{c} = 0$ is chosen, the nonlinear model reduces to the linear model.[2]

For illustrative purposes, the model (20) was fitted to the FEM data of the two-phase example machine, cf. Fig. 4(a). Fig. 6 shows the inverse inductances $\mathit{\Gamma}_\mathrm{d}$ and $\mathit{\Gamma}_\mathrm{q}$ and the equivalent MMF i_m at constant flux linkages as functions of the air gap. The characteristics obtained both from the FEM directly and from the fitted model are shown. It can be seen that the model (20) matches very well with the FEM results up to the air gap of about $y = 2.5$ mm. The selected order of the series expansion used in the model is sufficient to predict the behavior up to the air-gap values, which can be expected during operation. At larger air gaps, the behavior changes significantly due to the decreasing saturation effect, as demonstrated in Fig. 4(c).

[2] If desired, $\psi_\mathrm{d0}(y)$ could be solved from $\mathit{\Gamma}_\mathrm{d}(\psi_\mathrm{d0}, 0, y)\psi_\mathrm{d0} - i_\mathrm{m}(y) = 0$ in the saturated case. With (20), this is a cubic equation, leading to a complicated expression for F_y.

$$\sqrt{-\frac{1}{F_{\mathrm{y}}+\dfrac{b_{\mathrm{d}}[\psi_{\mathrm{d}}^2-\psi_{\mathrm{d0}}(y)^2]+b_{\mathrm{q}}\psi_{\mathrm{q}}^2}{2}+(b_{\mathrm{m}}+2b'_{\mathrm{m}}y)[\psi_{\mathrm{d}}-\psi_{\mathrm{d0}}(y)]}}=\theta_1+\theta_2 y \tag{24}$$

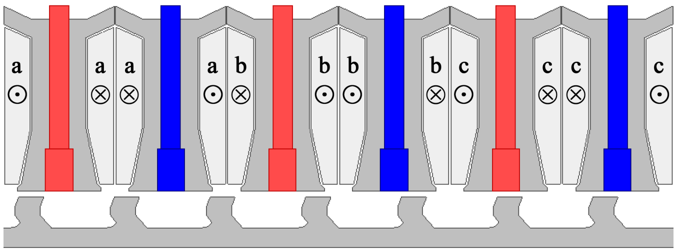

Fig. 7. Geometry of a prototype three-phase FSPM machine. The crosses and dots define the positive direction of the coil currents. This design is used in the FEM analysis and experiments.

TABLE I
FITTED MODEL PARAMETERS FOR
THE PROTOTYPE THREE-PHASE MACHINE

Parameter	Value	Unit
a_{d}	4.4	1/H
a_{q}	4.1	1/H
a_{c}	7.1	1/[H·(Vs)^2]
b_{d}	-0.32	1/(H·mm)
b_{q}	-0.21	1/(H·mm)
i_{m0}	3.8	A
b_{m}	-1.4	A/mm
b'_{m}	0.17	A/(mm)^2
f	6.0	kN
c	0.34	1/mm

IV. PARAMETER ESTIMATION

The parameters of the model depend on the machine geometry. However, the aim is not to calculate these parameters based on the dimensions of the machine, but rather to estimate them using the data from the FEM or from experiments. There are different methods to fit the model parameters. As an example, one fitting procedure is briefly explained in this section.

The model (20) is linear in parameters and it can be reformulated as a regression model

$$\boldsymbol{i}=\boldsymbol{\varphi}^{\mathrm{T}}\boldsymbol{\theta} \tag{22}$$

where the regressed variable is $\boldsymbol{i}=[i_{\mathrm{d}},i_{\mathrm{q}}]^{\mathrm{T}}$. The regressors and the parameter vector, respectively, are

$$\boldsymbol{\varphi}=\begin{bmatrix}\psi_{\mathrm{d}} & 0\\ 0 & \psi_{\mathrm{q}}\\ (\psi_{\mathrm{d}}^2+\psi_{\mathrm{q}}^2)\psi_{\mathrm{d}} & (\psi_{\mathrm{d}}^2+\psi_{\mathrm{q}}^2)\psi_{\mathrm{q}}\\ y\psi_{\mathrm{d}} & 0\\ 0 & y\psi_{\mathrm{q}}\\ -1 & 0\\ -y & 0\\ -y^2 & 0\end{bmatrix}\quad \boldsymbol{\theta}=\begin{bmatrix}a_{\mathrm{d}}\\ a_{\mathrm{q}}\\ a_{\mathrm{c}}\\ b_{\mathrm{d}}\\ b_{\mathrm{q}}\\ i_{\mathrm{m0}}\\ b_{\mathrm{m}}\\ b'_{\mathrm{m}}\end{bmatrix}. \tag{23}$$

Linear least squares (LLS) can be used to solve the parameter vector, if the data set $\{i_{\mathrm{d}}(n),i_{\mathrm{q}}(n),\psi_{\mathrm{d}}(n),\psi_{\mathrm{q}}(n),y(n)\}$, $n=1\ldots N$, is available. The number of samples N should be larger than the number of parameters. Thus, the parameter estimation problem reduces to solving a set of linear equations. Neither initial values nor cost functions are needed. As an alternative, fitting could be performed in multiple consecutive steps, as described in [21].

The normal-force expression (13) can also be reformulated as a regression model (24), shown at the top of this page. Hence, if the samples of F_{y} are known, the remaining two unknown parameters are obtained as $f=1/\theta_1^2$ and $c=\theta_2/\theta_1$ by means of the LLS method.

V. RESULTS

In this section, a prototype three-phase machine is analyzed by means of the FEM and experiments. Fig. 7 shows a part of the machine cross-section. The geometry is the result of the machine design optimization, aimed to improve the efficiency and material usage. The rail teeth shape is chosen to improve the thrust force generation in one x-axis direction (2.6% increase). This effect is small and thus not taken into account explicitly in the model. One machine unit consists of 12 mover slots and 14 rail poles. There are also additional teeth at both ends of the mover to minimize the end effects and to reduce the cogging force [22]. The additional teeth are included in the FEM model.

The flux linkages $(\psi_{\mathrm{d}},\psi_{\mathrm{q}})$ and the force components $(F_{\mathrm{x}},F_{\mathrm{y}})$ were solved as functions of the currents $(i_{\mathrm{d}},i_{\mathrm{q}})$ and the air gap y in predefined operating points using the static FEM [23]. The operating points were chosen to cover the whole operating range of the machine in terms of allowable currents and possible air-gap variation. The results of the FEM computation were used for estimating the parameters of the proposed model as described in Section IV. Table I gives the resulting parameters for the prototype three-phase machine. In the following subsections, the proposed model is invariably parametrized using the parameters of Table I.

A. Comparison of the Proposed Model to the FEM Data

The results predicted by the proposed model are compared to the FEM data in Figs. 8, 9, and 10. Most notable dependencies are shown. Fig. 8 shows the relationship between the flux linkages and the currents at selected constant air gaps. In the case of the proposed model, these characteristics are obtained from (14) and (20). Based on the FEM results, it was found out that both the d- and q-axes of the machine saturate strongly. It can be seen that the proposed model matches the FEM data very well.

Fig. 9 shows the presence of cross-saturation in the machine. The operating points simulated with the FEM are shown with blue markers. The 3D surfaces show that the proposed model is able to adequately take into account the cross-saturation phenomena, when fitted into the FEM data.

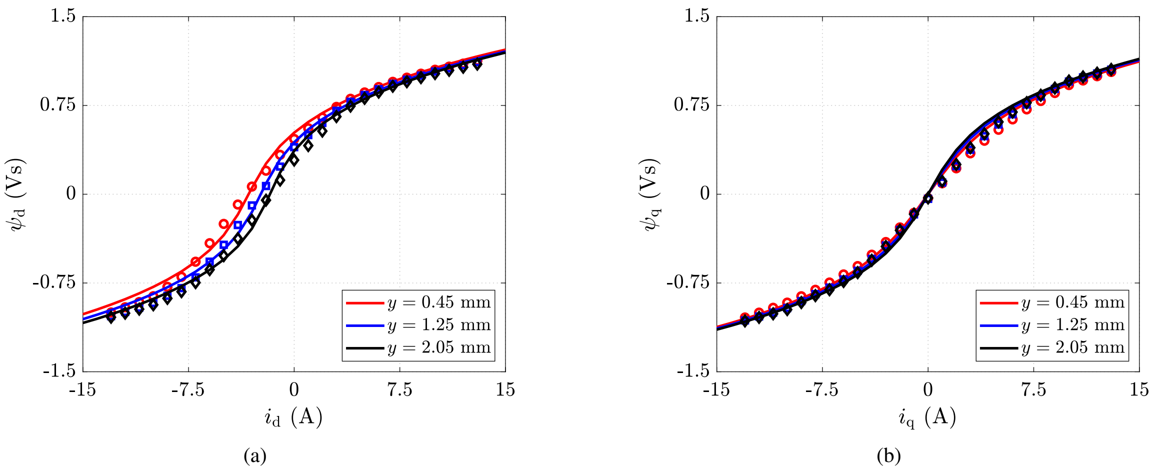

Fig. 8. Flux linkages as function of currents at constant air-gap values: (a) ψ_d as a function of i_d at $i_q = 0$; (b) ψ_q as a function of i_q at $i_d = 0$. The markers show the FEM results, and the solid lines show the results from the proposed model.

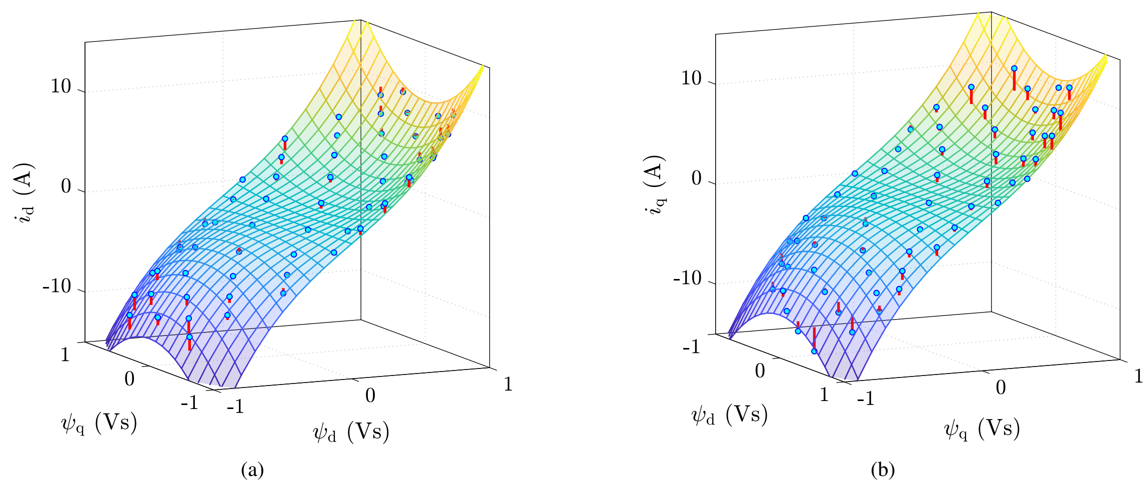

Fig. 9. Currents as function of flux linkages at constant air gap $y = 1.25$ mm: (a) i_d ; (b) i_q as a function of ψ_q and ψ_d. The blue circles represent the FEM results and the surfaces show the results from the proposed model. The red lines show the differences between the model and the FEM data.

Figs. 10(a) and 10(d) show the nonlinear dependency of the forces F_y and F_x on the current components i_d and i_q. It is also worth noticing that the forces were not fitted into the FEM force data, but rather calculated with (12) and (19) based on the fitted magnetic model parameters shown in Table I.

Figs. 10(b) and 10(e) show the forces F_x and F_y as functions of the air gap at constant dq currents. It can be seen that the model is able to predict the forces at close to zero air gap and at more than twice the nominal air gap. Figs. 10(c) and 10(f) show the forces F_x and F_y as functions of the mover position x at constant air gap $y = 1.25$ mm and at constant dq currents [which correspond to sinusoidally varying phase currents as a function of x, cf. (1) and (6)]. Based on the FEM, the effect of the x position on the forces is insignificant. Thrust force ripple is low, which is a common feature in FSPM machines [24]. It can also be seen that the proposed model predicts the force values with good accuracy. Overall, the characteristics of the proposed model are smooth, predictable, and physically consistent, which is important in control applications. The model was also fitted to the FEM data of another FSPM linear machine design, and the fitting showed equally good results.

B. Experiments

Fig. 11 shows the experimental setup. The mover consists of two converter-fed prototype machine units, whose geometry is shown in Fig. 7. The machine units are mounted in a double-sided configuration with the rails fixed on a stationary vertical beam. The nominal air gap of the system is 1.05 mm. The total mass of the mover is 100 kg. The maximum continuous current is 10 A. The nominal thrust force of each machine is 600 N. The nominal travel speed is 1 m/s.

The induced phase voltages of the prototype three-phase FSPM machine were measured at a constant mover velocity in a no-load condition ($i_d = i_q = 0$) at two mechanically fixed air-gap positions ($y = 0.5$ mm and $y = 2$ mm). Fig. 12 shows the corresponding phase flux linkages, calculated from the measured phase voltages. As expected, the phase flux linkages vary almost sinusoidally and depend on the air gap. Furthermore, the phase flux linkages include a clearly

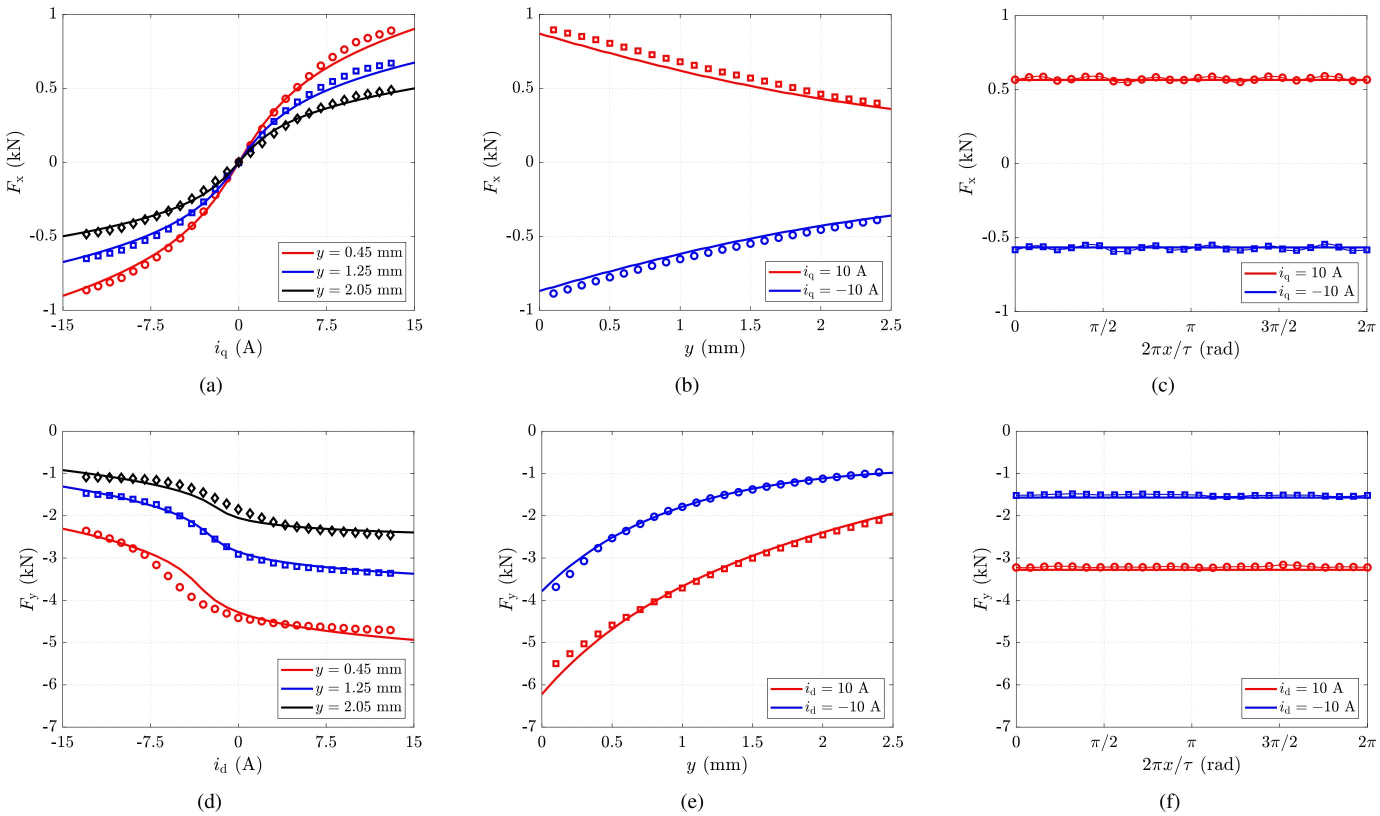

Fig. 10. Forces obtained from the FEM results (shown with markers) and from the model (shown with solid lines): (a) F_{x} as a function of i_{q} at $i_{\mathrm{d}} = 0$; (b) F_{x} as a function of the air gap y at $x = 0$ and $i_{\mathrm{d}} = 0$; (c) F_{x} as a function of the mover position x at $y = 1.25$ mm and $i_{\mathrm{d}} = 0$; (d) F_{y} as a function of i_{d} at $i_{\mathrm{q}} = 0$; (e) F_{y} as a function of the air gap y at $x = 0$ and $i_{\mathrm{q}} = 0$; (f) F_{y} as a function of the mover position x at $y = 1.25$ mm and $i_{\mathrm{q}} = 0$.

visible zero-sequence component, which originates from the additional flux-guiding teeth at both ends of the prototype machine unit [22]. However, since the zero-sequence current cannot flow in the three-phase winding without the neutral wire, the zero-sequence flux linkage does not contribute to the force production, and it does not need to be taken into account in the model. Fig. 12 also shows the corresponding phase flux linkages computed with the FEM (where the flux-guiding teeth were included) and with the proposed model. It can be seen that the results from the model match comparatively well with the measured and FEM results. The $\alpha\beta$ components match even better, since the zero-sequence component disappears in the transformation (1).

Fig. 13 presents the machine configuration that is used for measuring the attraction force. The mover could be levitated in the y direction by adjusting the currents of the two machine units. However, for the purposes of the force measurements, the mover was fixed into desired constant y positions using the four load cells, mounted at each corner of machine unit 1, and the differential normal force $\Delta F_{\mathrm{y}} = F_{\mathrm{y1}} - F_{\mathrm{y2}}$ was measured at different d-axis currents. The d-axes currents are selected to be $i_{\mathrm{d1}} = -i_{\mathrm{d2}}$ and varied between 0 and 12 A. The q-axis currents were kept at zero, $i_{\mathrm{q1}} = i_{\mathrm{q2}} = 0$.

The movement in the x direction was mechanically disabled by using a counterweight for compensating the gravitational force acting on the mover. In addition to ΔF_{y}, the air-gap lengths and the currents of both machine units were measured. The differential air gap is defined as $\Delta y = y_2 - y_1$. Naturally, the differential air gap is zero at the nominal air gap.

Fig. 14 shows the measured forces together with the forces from the FEM and from the proposed model at three differential air gaps ($\Delta y = -0.2$ mm, $\Delta y = -0.8$ mm, and $\Delta y = -1.4$ mm). It can be seen that the results from the experiments, FEM, and model match well. The forces from the FEM data and from the model differ more from the measured forces in the case of the largest air gap. The larger discrepancy between the measured and FEM-based forces at $i_{\mathrm{d1}} = 3$ A are due to the difference in the magnetic properties of the soft magnetic material used in the prototype and in the FEM model. Inaccuracies in the force measurement procedure and manufacturing tolerances also contribute to the discrepancy. However, the accuracy of the proposed model should be sufficient for model-based real-time control, as can be seen, e.g., from the results in [15].

VI. Conclusions

The magnetic characteristics of a linear bearingless FSPM machine were analyzed. Based on the magnetic equivalent circuit, a set of analytical equations in dq coordinates was derived to describe the currents and the force production of the machine. The effects of the air-gap variation and magnetic saturation were taken into account. The proposed model can be used for real-time control and estimation in bearingless drive systems. Due to its generality, the model can be easily applied to different machine designs. The model parameters can be estimated from the FEM or measured data. As an example, the

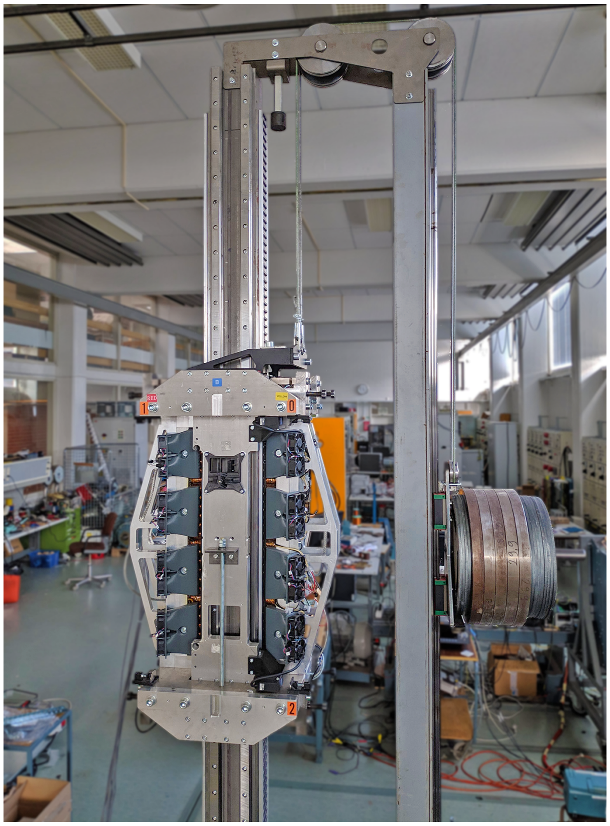

Fig. 11. Photo of the experimental setup showing a vertical double-sided rail with a mover composed of bearingless FSPM machines. The gravitational force acting on the mover is compensated with a counterweight.

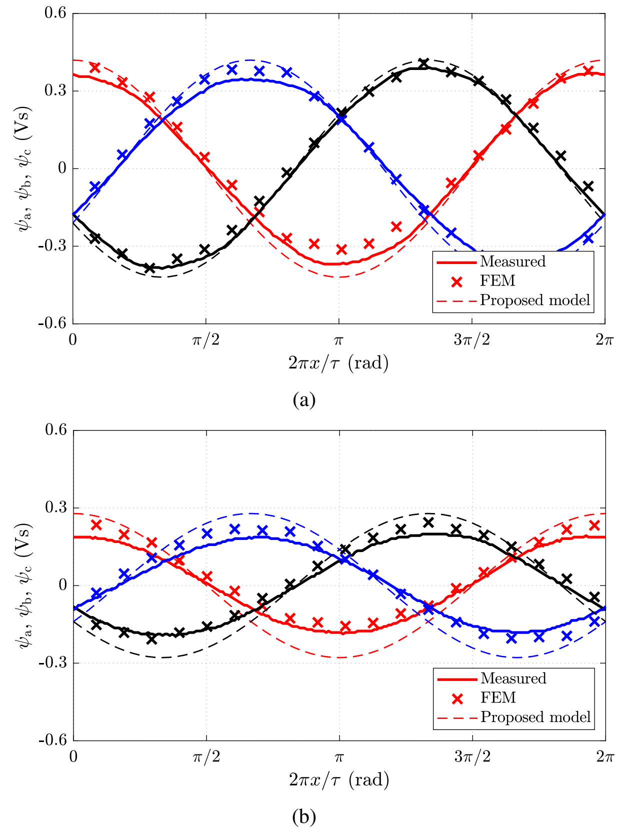

Fig. 12. Measured phase flux linkages as function of the mover position x at two air-gap values: (a) $y = 0.5$ mm; (b) $y = 2$ mm. For comparison, the results from the FEM and from the proposed model are also shown.

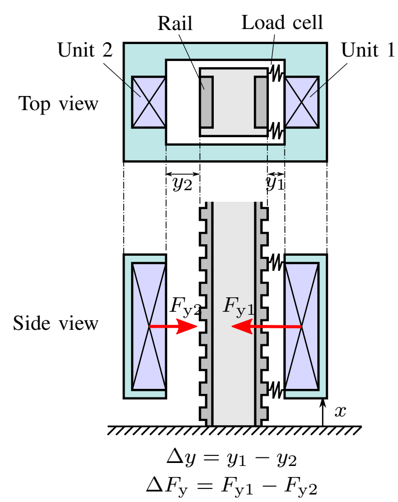

Fig. 13. Experimental configuration for measuring the differential normal force $\Delta F_{\rm y}$ of a double-sided bearingless FSPM machine, using four load cells located at each corner of machine unit 1. The differential air gap Δy and the d-axis currents $i_{\rm d1} = -i_{\rm d2}$ were varied.

proposed model was fitted to the FEM data computed for the three-phase prototype machine. The validity of the FEM data and the proposed model was evaluated by measuring the no-load flux linkages and normal forces of the prototype machine at different air-gap values.

Appendix
Analytical Expressions for the Conceptual Two-Phase Machine

The simplified magnetic equivalent circuit shown in Fig. 5 is considered. Since $a_{\rm s} \gg b_{\rm s}y$, we assume $b_{\rm s} = 0$ in the following derivation for simplicity. Using the standard circuit theory, all the fluxes of the circuit are solved as functions of $i_{\rm d}$, $i_{\rm q}$, and y. Then, the flux linkage $\psi_{\rm d}$ is obtained by summing the fluxes going through the d-axis MMF sources, assuming the two d-axis coils to be connected in series. The flux linkage $\psi_{\rm q}$ is solved similarly. These flux linkages expressions yield the inverse inductances (25), shown at the top of the next page.

From Fig. 5, the magnetic field energy w_0 at $\psi_{\rm d} = \psi_{\rm q} = 0$ can be derived using the circuit theory, as explained in [19]. The result is (16) with the constants

$$f = 8\phi_{\rm r}^2 b_{\rm t} \qquad c = \frac{a_{\rm m} + 4a_{\rm s}}{a_{\rm m}a_{\rm s}} b_{\rm t}. \tag{26}$$

The total field energy is given by (15). The analytical expression for the normal force could be calculated using (13), (15), and (25). However, this expression is very long and valid only for the geometry of the conceptual model without the magnetic saturation.

The expressions for the constant coefficients appearing in the series expansion (18) could be calculated from (25). The constants $a_{\rm d}$, $a_{\rm q}$, $b_{\rm d}$, $b_{\rm q}$, and $b'_{\rm m}$ are positive, while the constant $b_{\rm m}$ is negative for the conceptual model.

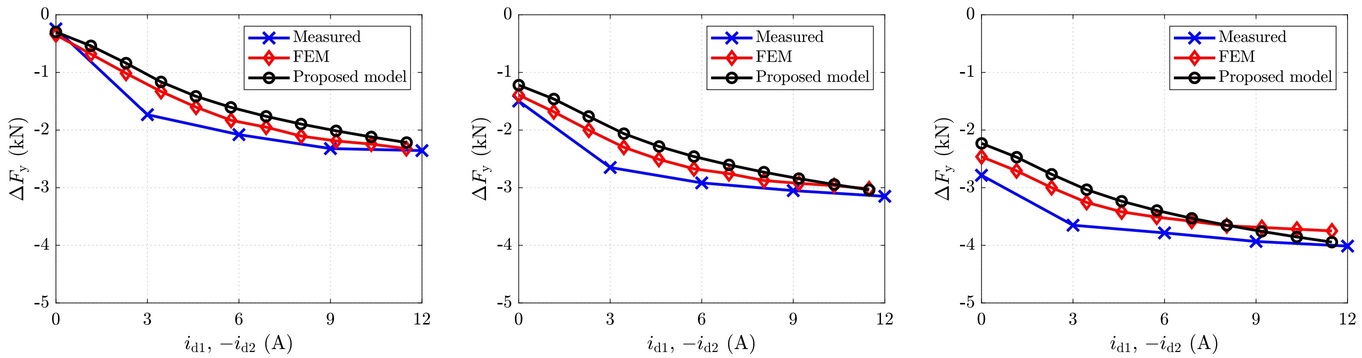

(a) $\Delta y = -0.2$ mm, $i_{\mathrm{d1}} = -i_{\mathrm{d2}}$ (b) $\Delta y = -0.8$ mm, $i_{\mathrm{d1}} = -i_{\mathrm{d2}}$ (c) $\Delta y = -1.4$ mm, $i_{\mathrm{d1}} = -i_{\mathrm{d2}}$

Fig. 14. Measured differential normal force ΔF_{y} as a function of the d-axis current: (a) $\Delta y = -0.2$ mm; (b) $\Delta y = -0.8$ mm; (c) $\Delta y = -1.4$ mm. For comparison, the results from the FEM and from the proposed model are also shown.

$$\mathit{\Gamma}_{\mathrm{d}}(y) = \frac{a_{\mathrm{m}}^2 a_{\mathrm{s}}^2 + 2a_{\mathrm{m}}a_{\mathrm{s}}(a_{\mathrm{m}} + 3a_{\mathrm{s}})b_{\mathrm{t}}y + (a_{\mathrm{m}}^2 + 6a_{\mathrm{m}}a_{\mathrm{s}} + 8a_{\mathrm{s}}^2)b_{\mathrm{t}}^2 y^2}{2[a_{\mathrm{m}}a_{\mathrm{s}}(2a_{\mathrm{m}} + 3a_{\mathrm{s}}) + 2(a_{\mathrm{m}}^2 + 5a_{\mathrm{m}}a_{\mathrm{s}} + 4a_{\mathrm{s}}^2)b_{\mathrm{t}}y + (3a_{\mathrm{m}} + 8a_{\mathrm{s}})b_{\mathrm{t}}^2 y^2]} \tag{25a}$$

$$\mathit{\Gamma}_{\mathrm{q}}(y) = \frac{a_{\mathrm{m}}a_{\mathrm{s}}^2 + 2a_{\mathrm{s}}(a_{\mathrm{m}} + a_{\mathrm{s}})b_{\mathrm{t}}y + (a_{\mathrm{m}} + 2a_{\mathrm{s}})b_{\mathrm{t}}^2 y^2}{2[a_{\mathrm{s}}(2a_{\mathrm{m}} + a_{\mathrm{s}}) + 2(a_{\mathrm{m}} + 3a_{\mathrm{s}})b_{\mathrm{t}}y + b_{\mathrm{t}}^2 y^2]} \tag{25b}$$

$$i_{\mathrm{m}}(y) = \frac{2[a_{\mathrm{m}}a_{\mathrm{s}}^2 + 2a_{\mathrm{s}}^2 b_{\mathrm{t}}y - (a_{\mathrm{m}} + 2a_{\mathrm{s}})b_{\mathrm{t}}^2 y^2]a_{\mathrm{m}}\phi_{\mathrm{r}}}{a_{\mathrm{m}}a_{\mathrm{s}}(2a_{\mathrm{m}} + 3a_{\mathrm{s}}) + 2(a_{\mathrm{m}}^2 + 5a_{\mathrm{m}}a_{\mathrm{s}} + 4a_{\mathrm{s}}^2)b_{\mathrm{t}}y + (3a_{\mathrm{m}} + 8a_{\mathrm{s}})b_{\mathrm{t}}^2 y^2} \tag{25c}$$

References

[1] E. Hoang, A. H. Ben-Ahmed, and J. Lucidarme, "Switching flux permanent magnet polyphased synchronous machines," in *Proc. EPE*, vol. 3, Trondheim, Norway, Sep. 1997, pp. 903–908.

[2] Z. Q. Zhu, Y. Pang, D. Howe, S. Iwasaki, R. Deodhar, and A. Pride, "Analysis of electromagnetic performance of flux-switching permanent-magnet machines by nonlinear adaptive lumped parameter magnetic circuit model," *IEEE Trans. Magn.*, vol. 41, no. 11, pp. 4277–4288, Nov. 2005.

[3] W. Gruber and K. Radman, "Modeling and realization of a bearingless flux-switching slice motor," *Actuators*, vol. 6, no. 12, Mar. 2017.

[4] A. Chiba, T. Fukao, O. Ichikawa, M. Oshima, M. Takemoto, and D. G. Dorrell, *Magnetic Bearings and Bearingless Drives*, 1st ed. Burlington, MA: Newnes, 2005.

[5] C. F. Wang, J. X. Shen, L. L. Wang, and K. Wang, "A novel permanent magnet flux-switching linear motor," in *Proc. IET PEMD*, York, U.K., Apr. 2008, pp. 116–119.

[6] M.-J. Jin, C.-F. Wang, J.-X. Shen, and B. Xia, "A modular permanent-magnet flux-switching linear machine with fault-tolerant capability," *IEEE Trans. Magn.*, vol. 45, no. 8, pp. 3179–3186, Aug. 2009.

[7] L. Huang, H. Yu, M. Hu, J. Zhao, and Z. Cheng, "A novel flux-switching permanent-magnet linear generator for wave energy extraction application," *IEEE Trans. Magn.*, vol. 47, no. 5, pp. 1034–1037, May 2011.

[8] R. Cao, M. Cheng, C. Mi, W. Hua, X. Wang, and W. Zhao, "Modeling of a complementary and modular linear flux-switching permanent magnet motor for urban rail transit applications," *IEEE Trans. Energy Convers.*, vol. 27, no. 2, pp. 489–497, Jun. 2012.

[9] L. Huang, H. Yu, M. Hu, and H. Liu, "Study on a long primary flux-switching permanent magnet linear motor for electromagnetic launch systems," *IEEE Trans. Plasma Sci.*, vol. 41, no. 5, pp. 1138–1144, May 2013.

[10] T. Purosto, T. Hakala, J. Ratia, and I. Petrov, "Elevator with linear motor," U.S. Patent Appl. 2018/0 105 396 (A1), Apr. 19, 2018.

[11] T. Korhonen, T. Hakala, P. Raassina, S. Suur-Askola, M. Hinkkanen, S. Saarakkala, M. Sokolov, and R. Hosseinzadeh, "Electric linear motor," U.S. Patent Appl. 2019/0 300 329 (A1), Oct. 3, 2019.

[12] S. Zhou, H. Yu, M. Hu, C. Jiang, and L. Huang, "Nonlinear equivalent magnetic circuit analysis for linear flux-switching permanent magnet machines," *IEEE Trans. Magn.*, vol. 46, no. 2, pp. 882–886, Feb. 2012.

[13] S. R. Aleksandrov, L. Wang, D. T. E. H. van Casteren, J. J. H. Paulides, and E. A. Lomonova, "Semi-analytical analysis of rotating and linear flux-switching PM machines including skewing," in *Proc. EVER*, Monte Carlo, Monaco, Apr. 2017.

[14] R. P. Jastrzebski, P. Jaatinen, and O. Pyrhönen, "Modeling and control design simulations of a linear flux-switching permanent-magnet-levitated motor," *Mechanical Engineering Journal*, vol. 4, no. 5, Jul. 2017.

[15] S. E. Saarakkala, M. Sokolov, R. Hosseinzadeh, and M. Hinkkanen, "Levitation control for a double-sided bearingless linear motor based on feedback linearization," in *Proc. IEEE ECCE*, Baltimore, MD, Oct. 2019.

[16] M. Sokolov, S. E. Saarakkala, R. Hosseinzadeh, and M. Hinkkanen, "Modeling of a bearingless flux-switching permanent-magnet linear motor," in *Proc. IEEE ITEC*, Long Beach, CA, Jun. 2018.

[17] H. H. Woodson and J. R. Melcher, *Electromechanical Dynamics: Part I: Discrete Systems*. New York: John Wiley & Sons, 1968, Massachusetts Institute of Technology: MIT OpenCourseWare. [Online]. Available: http://ocw.mit.edu

[18] A. E. Fitzgerald, C. Kingsley, Jr., and S. D. Umans, *Electric Machinery*, 6th ed. Boston, MA: McGraw-Hill, 2003.

[19] D. Meeker, "Magnetic circuit derivation of energy stored in a permanent magnet," Apr. 2007. [Online]. Available: http://www.femm.info/wiki/pmenergy

[20] J. Fischer and U. Moser, "Die Nachbildung von Magnetisierungskurven durch einfache algebraische oder transzendente Funktionen," *Archiv für Electrotechnik*, vol. 42, no. 5, pp. 286–299, 1956.

[21] M. Hinkkanen, P. Pescetto, E. Mölsä, S. E. Saarakkala, G. Pellegrino, and R. Bojoi, "Sensorless self-commissioning of synchronous reluctance motors at standstill without rotor locking," *IEEE Trans. Ind. Appl.*, vol. 53, no. 3, pp. 2120–2129, May/Jun. 2017.

[22] Y. Du, G. Yang, L. Quan, X. Zhu, F. Xiao, and H. Wu, "Detent force reduction of a c-core linear flux-switching permanent magnet machine with multiple additional teeth," *Energies*, vol. 10, no. 3, 2017.

[23] S. E. Saarakkala, M. Sokolov, V. Mukherjee, J. Pippuri, K. Tammi, A. Belahcen, and M. Hinkkanen, "Flux-linkage model including cross-saturation for a bearingless synchronous reluctance motor," in *Proc. 15th International Symposium on Magnetic Bearings (ISMB15)*, Kitakyushu, Japan, Aug. 2016.

[24] R. Cao, C. Mi, and M. Cheng, "Quantitative comparison of flux-switching permanent-magnet motors with interior permanent magnet motor for EV, HEV, and PHEV applications," *IEEE Trans. Magn.*, vol. 48, no. 8, pp. 2374–2384, Aug. 2012.

Maksim Sokolov received the B.Sc.(Tech.) and M.Sc.(Tech.) degrees in electrical engineering from the ITMO University, Saint Petersburg, Russia, in 2012 and 2014, respectively. He is currently working toward the D.Sc.(Tech.) degree at Aalto University, Espoo, Finland.

His main research interests include control of electric drives, bearingless machines, and magnetic levitation.

Seppo E. Saarakkala received the M.Sc.(Eng.) degree in electrical engineering from the Lappeenranta University of Technology, Lappeenranta, Finland, in 2008, and the D.Sc.(Tech.) degree in electrical engineering from Aalto University, Espoo, Finland, in 2014.

He has been with the School of Electrical Engineering, Aalto University, since 2010, where he is currently a Post-Doctoral Research Scientist. His main research interests include control systems and electric drives. He was the recipient of the 2018 IEEE Industry Applications Society Industrial Drives Committee Best Paper Award.

Reza Hosseinzadeh received the B.Sc.(Eng.) degree in electrical engineering from the Islamic Azad University (IAU), Bushehr, Iran, in 2009, and the M.Sc.(Tech.) degree in electrical engineering from Aalto University, Espoo, Finland, in 2019. He is currently working toward the D.Sc.(Tech.) degree at Aalto University.

His main research interests include bearingless motors, electric drives, and control systems.

Marko Hinkkanen (M'06–SM'13) received the M.Sc.(Eng.) and D.Sc.(Tech.) degrees in electrical engineering from the Helsinki University of Technology, Espoo, Finland, in 2000 and 2004, respectively.

He is currently an Associate Professor with the School of Electrical Engineering, Aalto University, Espoo, Finland. His research interests include control systems, electric drives, and power converters.

Dr. Hinkkanen was a General Co-Chair for the 2018 IEEE 9th International Symposium on Sensorless Control for Electrical Drives (SLED). He was the recipient of the 2016 International Conference on Electrical Machines (ICEM) Brian J. Chalmers Best Paper Award and the 2016 and 2018 IEEE Industry Applications Society Industrial Drives Committee Best Paper Awards. He is an Associate Editor for the IEEE TRANSACTIONS ON ENERGY CONVERSIONS and the *IET Electric Power Applications*.